A&A 451, 1133–1137 (2006)
DOI: 10.1051/0004-6361:20054296

Astronomy & Astrophysics

First sky validation of an optical polarimetric interferometer⋆,⋆⋆

K. Rousselet-Perraut[1], J. B. Le Bouquin[1], D. Mourard[2], F. Vakili[3], O. Chesneau[2], D. Bonneau[2], J. L. Chevassut[2], A. Crocherie[2], A. Glentzlin[2], S. Jankov[3], S. Ménardi[4], R. Petrov[3], and C. Stehlé[5]

[1] Laboratoire d'Astrophysique de l'Observatoire de Grenoble, BP 53, 38041 Grenoble Cedex 9, France
e-mail: Karine.Perraut@obs.ujf-grenoble.fr
[2] Observatoire de la Côte d'Azur, Département Gemini, Avenue Copernic, 06130 Grasse, France
[3] Laboratoire Universitaire d'Astrophysique de Nice, UNSA, Faculté des Sciences, 06108 Nice Cedex 02, France
[4] ESO, Karl-Schwarzschild-Str. 2, 85748 Garching bei München, Germany
[5] Laboratoire de l'Univers et de ses THéories, UMR 8102, Observatoire de Paris, 5 place Jules Janssen, 92195 Meudon, France

Received 3 October 2005 / Accepted 10 January 2006

ABSTRACT

Aims. We present the first lab and sky validation of spectro-polarimetric equipment put at the combined focus of an optical long-baseline interferometer. We tested the polarimetric mode designed for the visible GI2T Interferometer to offer spectropolarimetric diagnosis at the milliarcsecond scale.
Methods. We first checked the whole instrumental polarization in the lab with a fringe simulator, and then we observed α Cep and α Lyr as stellar calibrators of different declinations to tabulate the polarization effects throughout the GI2T declination range.
Results. The difference between both linear polarizations is within the error bars and the visibilities recorded in natural light (i.e. without the polarimeter) for calibration purposes are the same order of magnitude as the polarized ones. We followed the α Cep visibility for 2 h after the transit and α Lyr for 1.5 h and detected no decrease with hour angle due to the fringe pattern smearing by instrumental polarization.
Conclusions. Differential celestial rotation due to the dissymetric Coudé trains of the GI2T is well-compensated by the field rotators, so the instrumental polarization is controlled over a relatively wide hour angle range (±2 h around the transit at least). Such a polarimetric mode opens new opportunities especially for studies of circumstellar environments and significantly enhances both the potential of an optical array and its ability for accurate calibration.

Key words. technique: interferometric – instrumentation: interferometers – techniques: polarimetric

1. Introduction

Light polarization is a key in understanding the physics of many astrophysical phenomena occuring on the Sun, in particular magnetized plasmas of A and B stars, in disks surrounding young stellar objects and in hot stellar winds, active galactic nuclei, black holes, interstellar medium, etc. Spectropolarimetry offers a powerful diagnostic potential for addressing these issues even if the interpretation remains limited by the lack of spatial resolution.

Coupling high angular resolution to spectropolarimetry is thus very attractive but also very challenging as illustrated by the first attempts to detect astrophysical polarization by optical long-baseline interferometry. At the beginnings of modern interferometry, Hanbury Brown et al. (1974) tried to detect the diameter variation of β Orionis versus linear polarization. The same experiment was carried out again on α Lyr by Vakili (1981) and on γ Cas by Rousselet-Perraut et al. (1997). But all of these observations were strongly limited by poor signal-to-noise ratios whose limitations were clearly greater than the amplitude of the expected signals. In fact, long baselines (and thus high angular resolutions) are mandatory when correctly detecting local polarized structures, which are typically smaller than the stellar diameter. If the angular resolution is not large enough, relevant signals are diluted over large-scale structures as the net polarization is averaged over the stellar disk in classical polarimetry. As a consequence high accuracy has to be reached on each measurement point. Moreover, such detection of local polarized features requires close control of the instrumental polarization to prevent it from dominating the measured signals.

Parallel to these preliminary observations, several theoretical studies have been conducted based on different formalisms (Rousselet-Perraut et al. 1996; Elias 2004; Tinbergen 2003) to describe the effects of instrumental polarization on the interferometric observables. These works clearly show that, whatever the observing mode, we need to design interferometers by paying attention to the polarization that can strongly degrade the interferometric performance. Within this context of both instrumental polarization modelling for interferometers and detection of the astrophysical polarization with better spatial resolution, the GI2T/REGAIN was designed with minimal instrumental polarization and with a polarimetric mode inside its spectrograph (Mourard et al. 2003). As such, it is the only equipment providing spectro-polarimetry at the 1-milliarcsecond (mas) angular resolution that allows investigation of mass-loss events from hot stars (Chesneau & Wolf 2003), inhomogeneous circumstellar materials (Vakili et al. 1997), or magnetic field topologies (Rousselet-Perraut et al. 2004).

⋆ Based on observations collected at the Grand Interféromètre à 2 télescopes, Observatoire de la Côte d'Azur, France.
⋆⋆ Appendices A and B are only available in electronic form at http://www.edpsciences.org

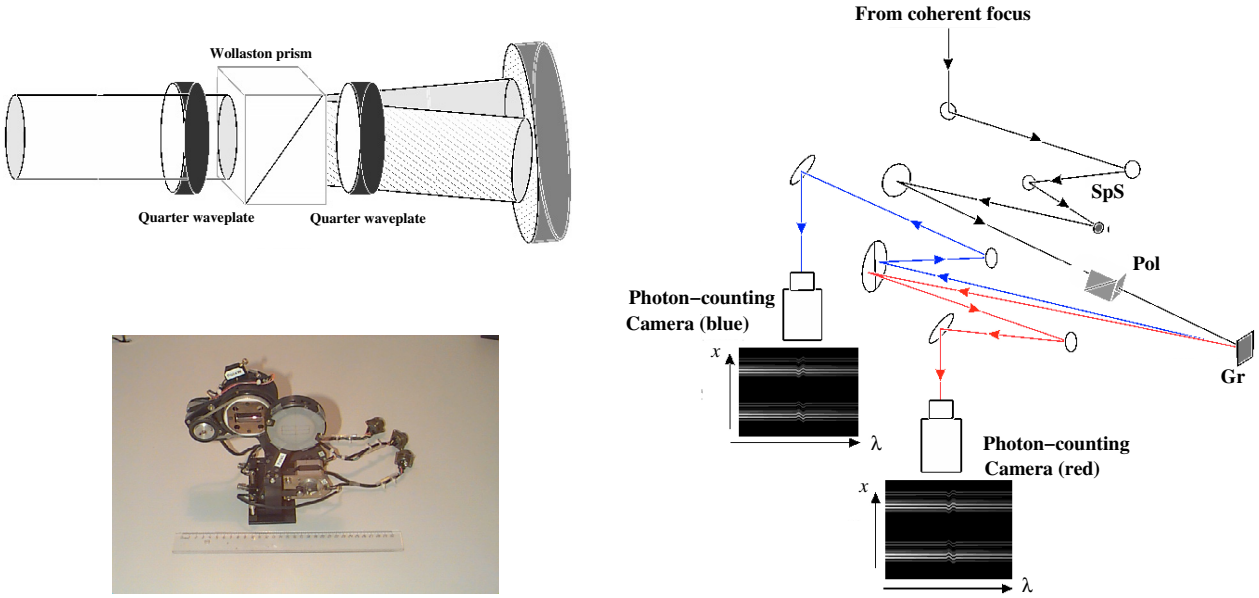

Fig. 1. *Left.* Sketch (*top*) and front-view photograph (*bottom*) of the polarimetric mode (Pol) included in the GI2T/REGAIN spectrograph placed at the combined focus of the interferometer. *Right.* GI2T/REGAIN spectrograph: after the spectrograph slit (SpS), light is collimated, goes eventually through the Wollaston prism and the quarter waveplates of the polarimeter (Pol), and is then dispersed by a diffraction grating (Gr) and detected on blue and red cameras. The (x, λ) images including spatial (x) and spectral (λ) information are recorded. An image is composed of either a naturally dispersed fringe pattern centered on the detectors or of two polarized dispersed fringe patterns placed at the top and the bottom of the detectors as displayed in this figure.

Chesneau et al. (2000) described the scientific rationale of such an instrument, and the new opportunities opened by polarimetric interferometry in the field of Miras are given in Ireland et al. (2005), who recently managed to measure optical polarimetric signals with the SUSI interferometer on Miras R Car and RR Sco and in modelling the calibrated visibilities to produce scientific results (dust-scattering location). Detailing the astrophysical issues is not the scope of this paper, which instead describes the lab qualification of this polarimetric mode after explaining the GI2T/REGAIN concept (Sect. 2). Then we analyze the visibilities in polarized light obtained on two stellar calibrators over an hour-angle range of about 2 h (Sect. 4) and emphasize the requirements for future interferometric instrumentation in terms of polarimetric performance.

2. The polarimetric mode of the GI2T

2.1. The instrument

The GI2T/REGAIN interferometer of the Observatoire de la Côte d'Azur in Southern France allows two 1.5-m telescopes to be combined in the visible along a North-South baseline up to 65 m long (Mourard et al. 2003). It is equipped with a spectrograph with three spectral resolutions reaching 30 000. It is a multispeckle dispersed-fringe interferometer that records (x, λ) images in its photon-counting detectors (Fig. 1) and thus provides visibility and differential phase for different spectral channels. A polarimetric mode was designed to allow astrophysical observations by spectro-polarimetric interferometry (Chesneau et al. 2000).

This polarimeter is mainly composed of a Wollaston prism to separate two orthogonal polarization states and of a movable quarter waveplate (Fig. 1-left). The polarimeter is placed inside the GI2T spectrograph, just before the grating wheel (Fig. 1-right). To avoid unbalanced transmissions of the polarization states by the grating, a fixed quarter waveplate is assembled after the Wollaston prism in the same mechanical mount to transform the two linearly polarized output beams in two circularly polarized ones that are affected by the same throughput factor by the grating grooves. The Wollaston prism is made of calcite and provides a beam angular separation of 0.37° to avoid beam vignetting on the camera. Quarter waveplates are made of three thin glass plates to reduce the chromatic effects as much as possible: the phase shift of $\lambda/4$ is given at ±3% throughout the [0.4 μm; 0.7 μm] spectral range.

After being spectrally dispersed, the two beams carrying both the interference and the polarization information are focused on a photon-counting camera that contains two (x, λ) images, one per polarization state referred to as *High* and *Low* with respect to their position on the detector (Fig. B.1a).

2.2. The output signals

At the polarimeter level, when the first quarter waveplate is removed, the Wollaston prism provides two linearly polarized orthogonal states of polarization (hereafter called parallel and perpendicular). When the quarter waveplate is inserted before the Wollaston prism, the latter provides two output beams corresponding to the two-incident circularly-polarized states (commonly referred to as left and right). In the classical polarimetric techniques, such a device gives access to three (I, Q, and V) of the four Stokes parameters. The Stokes vector has four real components (I, Q, U, V) expressed in terms of intensity corresponding to the observables of the polarization ellipse: I describes the total intensity of the light, Q the amount of linear horizontal and vertical polarization, U the amount of linear +45° and −45° polarization, and V the amount of right and left circular polarization contained within the beam (Collett 1992).

Such an interferometer equipped with a spectro-polarimeter allows measurement of interferometric observables (fringe contrast and fringe phase) in each spectral channel and in two perpendicular polarizations. Differential methods between

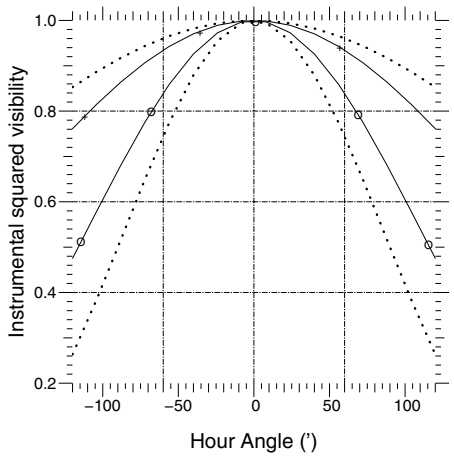

Fig. 2. Instrumental squared visibility versus hour angle for observations with the GI2T without correcting for differential celestial rotation at various declinations: the extreme declinations of the GI2T $\delta = 20°$ and 70° (dotted lines), the declination $\delta = 38°47'$ of α Lyr (∘), and the declination $\delta = 62°35'$ of α Cep (+).

two spectral channels or between two polarizations can be applied to produce differential phase and differential visibility measurements (Rousselet-Perraut et al. 2004).

2.3. Instrumental polarization modelling

The GI2T/REGAIN has been described in detail in several papers, (Mourard et al. 2003) for instance, so we focus here on its main characteristics in terms of polarization. Because of the telescope's design, the instrument presents asymmetric Coudé trains characterized by:

- a relatively small number of mirrors (13 from the primary mirror to the beam combiner);
- telescope tertiary mirrors with large incident angles ranging from 25° to 65° according to the telescope, the target declination, and the hour angle;
- a differential celestial rotation between the North and South telescopes ($\theta_n - \theta_s$) compensated for by field rotators.

The large and different incident angles on the tertiary mirrors lead to phase shifts between the two linear polarization directions that differ from one telescope to another, hence to a differential instrumental polarization between the two arms, to which the differential celestial rotation $\theta_n - \theta_s$ is added. These combined effects induce visibility losses due to the smearing of the various polarized fringe patterns and thus strongly reduce the hour-angle range of observations (Rousselet-Perraut et al. 1996). As displayed in Fig. 2, losses in squared visibility of about 15% were observed ±2 h around the transit for 70°-declination targets. These losses reached 75% at ±2 h around the transit for 20°-declination targets. To overcome this strong limitation, a field rotator composed of a three-mirror K-prism was designed to compensate for both differential field rotation and instrumental polarization (Rousselet-Perraut et al. 1998).

After the polarization optimization by means of the rotator coatings, residual effects remain due to the differential rotation of the polarization directions leading to squared visibility losses smaller than 17% throughout the 20° to 70° declination range and for observations carried out over ±4 h around the transit. The larger losses are reached for small declinations, i.e. when the differential rotation between the two arms is larger.

2.4. Calibrations

At the polarimeter level, the Wollaston prism can rotate from a 0°-position to a 180°-position so as to substract the potential bias due to the detector. The same state of polarization can be imaged on two different detector sub-windows since a 180°-rotation of the Wollaston inverts the two output beam positions on the detector. The whole device (the Wollaston prism and the two waveplates) can be removed for calibration purposes by means of measurement in natural light (a single interferogram at the detector center was observed in this case, Fig. B.1a), which have to bracket measurements in polarized light. All these movements were driven via the interferometer software, but nothing was moving during a sequence of acquisitions on a stellar source.

Observations were composed of a sequence of acquisitions on a scientific target bracketed with sequences of acquisitions on a calibrator, which is generally an unresolved source for the observation baseline so as to calibrate the interferometer answer to a point-like source (instrumental impulsional answer). It has to be close to the scientific target, with a similar spectral type, and unpolarized as much as possible, which is not mandatory if the calibrator is unresolved, as an unresolved target will lead to a visibility equal to 1, *whatever its intrinsic polarization*. Finally, for differential measurements between two close spectral channels, a calibrator is not mandatory.

2.5. Assembly, integration, and tests

To correctly transform linearly polarized into circularly polarized light, the neutral axes of a quarter waveplate have to be set at 45° with respect to the neutral axes of the Wollaston prism (i.e. the horizontal and vertical axes). These internal adjustments were performed with a dedicated lab workbench that allowed us to select the polarization of the incident beam and to accurately balance the flux between the two beams at the output of the Wollaston prism. This balance was checked through various spectral filters (B, V, and R) to refine the adjustment. Then the polarimeter was inserted in the spectrograph and its position adjusted by autocollimation. Then a flat mirror was fixed at the polarimeter output and the slit image reflected by this collimation mirror was used to adjust the tip, the tilt, and the slope of the polarimeter mount (since the spectrograph design induces a non horizontal optical axis).

A fringe simulator inside the REGAIN table allowed 1/ the lab performances of the polarimeter to be checked and 2/ the instrumental polarization of the whole instrument to be studied: a same laboratory white-light source was injected in each arm of the interferometer at the REGAIN table entrance and fringes were produced at the coherent focus. These fringes could be analyzed and recorded for different spectral channels and different polarization states. Moreover a linear sheet-film polarizer was introduced at the spectrograph entrance to study the instrumental polarization of the Coudé trains. This internal simulator operates with an Airy Disk, which makes alignment much more stringent than in the case of sky observations and light injection in the spectrograph entrance slit critical. Any mechanical drift of the simulator induces large rms fluctuations of the polarized visibilities. Despite this limitation, the main characteristics of the polarimetric mode were checked and/or studied during July 2002 with this workbench (Appendix A), when neither cross-talk effects between the two orthogonal polarization directions larger than 4×10^{-3} nor any drastic effect of instrumental polarization were observed.

Table 1. Journal of observations of polarimetric calibrators with the GI2T/REGAIN obtained on July 29, 2004. The columns from left to right give: the file number, the kind of observation either in natural light (Nat) or in linearly polarized light (Pol), the average hour angle with respect to the meridian transit HA, the projected baseline B_p, the projected angle PA, the squared visibility μ^2, the comments on file quality from observations and data-processing logs. Visibilities are not calibrated but only corrected for the main instrumental effects (see Appendix B).

File	Type	HA	B_p (m)	PA (°)	μ^2			Comments
					Low	*Nat*	*High*	
αLyr ($\delta = 38°47'$)								
1	Nat	–57′	13.611	–9	–	–	–	Bad fit of speckle and fringe peaks
2[a]	Nat	–52′	13.654	-8		0.11 ± 0.02		
3	Pol	–38′	13.754	–6	–	–	–	No photons
4	Pol	–31′	13.792	–5	–	–	–	No photons
5	Nat	–12′	13.857	–2		0.13 ± 0.02		
6	Pol	+18′	13.843	3	0.11 ± 0.02		0.15 ± 0.01	
7[a]	Pol	+25′	13.819	4	0.1 ± 0.1		0.14 ± 0.04	
8[a]	Pol	+32′	13.787	5	0.13 ± 0.04		0.15 ± 0.04	
αCep ($\delta = 62°35'$)								
1	Nat	+7′	20.110	2	–	–	–	No fringe tracking
2	Nat	+14′	20.104	3		0.22 ± 0.02		
3	Pol	+24′	20.089	5	0.26 ± 0.08		0.29 ± 0.04	
4	Nat	+34′	20.065	8		0.25 ± 0.03		
5	Pol	+45′	20.031	10	–	–	–	
6	Nat	+55′	19.991	12		0.262 ± 0.009		
7	Pol	+1h06′	19.939	15	–	–	–	Bat fit of fringe peak
8	Nat	+1h17′	19.879	17	–	–	–	No fringe tracking
9	Pol	+1h27′	19.817	20	–	–	–	Bat fit of fringe peak
10	Nat	+1h36′	19.756	22	–	–	–	No fringe tracking
11	Nat	+1h39′	19.735	22		0.26 ± 0.01		
12	Pol	+1h47′	19.675	24	–	–	–	No fringe tracking
13	Pol	+1h49′	19.660	25	0.3 ± 0.1		0.32 ± 0.03	
14	Nat	+2h01′	19.563	27		0.29 ± 0.01		
15	Pol	+2h12′	19.469	30	0.3 ± 0.1		0.29 ± 0.04	

[a] A neutral density (ND) of 0.3 has been inserted.

3. Observations

3.1. Journal of observations

We observed two polarimetric calibrators (i.e. without known polarized features) with short baselines of the GI2T (Table 1). They were chosen to cover the declination range of the GI2T since the instrumental polarization effects theoretically change with declination.

- α *Lyr* (HD 172167) is a well-known A0V star whose angular diameter was first measured by interferometry by Hanbury Brown et al. (1974) ($\Phi = 3.08 \pm 0.07$ mas). This star is very bright ($m_V = 0$) and slightly resolved at the shorter baseline of the GI2T: the expected visibility at a wavelength of 0.65 μm equals 0.878 ± 0.005 for a 14-m baseline. It is surrounded by a dusty debris disk whose flux at our wavelength is about a factor 1200 smaller than the photospheric one (Absil et al. 2006). The effect of the disk on the visibility in our configuration is thus negligible considering that visibility accuracy is a few percent. We thus adopted α Lyr as a calibrator for intermediate declinations ($\delta = 38°47'$).
- α *Cep* (HD 203280) is a A7IV-V rapid rotator ($v \sin i \sim 280$ km s^{-1}). It is a bright star in the visible ($m_V = 2.4$), whose angular dimensions were recently measured by van Belle et al. (2005) at 2.2 μm. Thanks to a wide coverage in hour angle, the authors determine a polar uniform disk diameter of $\Phi_p = 1.625 \pm 0.056$ mas and an equatorial uniform disk diameter of $\Phi_p = 1.355 \pm 0.080$ mas. Given our baseline of about 20 m, a position angle (PA) ranging from 2° and 30°, such an oblateness induces a visibility variation of a fraction of a percent throughout our hour angle range. We thus adopted α Cep as a good calibrator for large declinations ($\delta = 62°35'$).

Both targets were observed close to the Hα hydrogen line with the medium spectral resolution mode ($R = 5460$). The dispersed fringes were recorded as a series of data both in natural light (when the polarimeter was removed) and in linearly polarized light (when the polarimeter was inserted). For calibration purposes, observation in polarized light (called *Pol*) and observation in natural light (called *Nat*) succeeded one another. All the recorded data correspond to 20 ms short exposures for freezing the atmospheric turbulence. During recording, a fringe tracker had servo-controlled the fringe position, and furthermore we only considered those files for which the fringes were tracked. For this reason and also for weather conditions, the numbers of files varied from one target to another (Table 1). As a consequence, the hour-angle coverage was segmented and the observation sequence *Nat/Pol/Nat* was not always achieved.

3.2. Data processing

We reduced the data following the spectral density method described in Mourard et al. (1994). Due to a recent change of REGAIN detectors, we were obliged to define a slightly different visibility estimator, which allowed us to compare all the observations (natural and polarized ones) of a given target but *not* to discuss the absolute values of the visibility. Since we only looked for a visibility decrease with hour angle (due to instrumental polarization) and not for an accurate absolute value of the visibility, we considered the μ^2 estimations given in Sect. B.3 corresponding to visibilities only corrected for

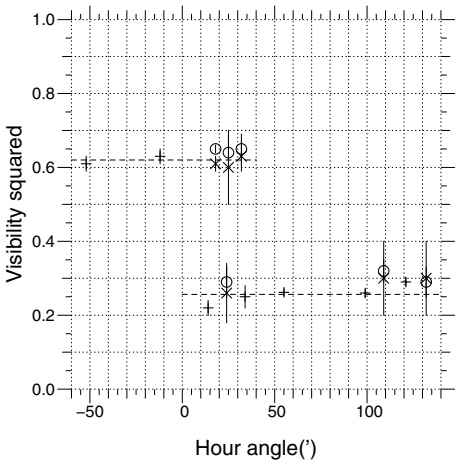

Fig. 3. *Natural* (+), *High* (∘), and *Low* (×) squared visibility versus hour angle obtained on α Lyr (*top*) and on α Cep (*bottom*) during the July 29, 2004 observations. The dash on the visibility curves gives the average of the *Natural* squared visibility for each data set. α Lyr visibilities squared have been shifted by 0.5. Visibilities are not calibrated but only corrected for main instrumental effects (see Appendix B).

main instrumental effects such as centroiding hole effect, photon bias, and pupil displacement.

4. Sky validation

4.1. Polarized visibilities for two declinations

We considered all the files that are unflagged and for which the statistical analysis of estimated energies were fine (see Appendix B.2.), and we derived the squared visibilities μ^2 for the two polarimetric calibrators (Table 1). For both objects, the difference between both polarizations is within the error bar, even if the *Low* visibilities generally remain slightly smaller than the *High* ones. The visibilities recorded in natural light (i.e. without the polarimeter) are within the same order of magnitude as the polarized ones.

4.2. Polarized visibilities vs. hour angle

We observed α Cep up to 2 h after the transit and α Lyr during around an hour and a half so as to follow the visibility variations with respect to hour angle (Fig. 3).

For α Cep, the *Nat* squared visibility was constant throughout the 2h-long observations: the average over the 5 files gives a mean squared visibility of 0.26 ± 0.03. The μ^2 decrease of 24% from the transit up to 2 h (Fig. 2) predicted by the modelling of the differential celestial rotation was not observed. This differential celestial rotation that generates instrumental polarization smearing the fringe patterns is thus well-compensated by the field rotators. Polarized visibilities (*High* and *Low*) seem not to vary with hour angle: throughout the 2h-long observations, the mean squared visibility equaled 0.29 ± 0.02 for the *Low* polarization and 0.30 ± 0.01 for the *High* one, which is comparable to the *Nat* value.

Due to the lower declination of α Lyr, the differential celestial rotation between the North and South telescopes was large, even 1 h before or after the transit (Fig. 2). Without instrumental polarization correction by field rotators, a μ^2 decrease of 16% was expected throughout the hour angle range of observations. Such a decay was not observed and observations presented the same trend as those of α Cep: the mean squared visibility equals 0.11 ± 0.05 for the *Low* polarization, 0.15 ± 0.03 for the *High* one, which is comparable to the *Nat* value (0.12 ± 0.02) with respect to the error bars. We conclude that residual instrumental polarization effects are very light, if any.

5. Conclusion

We have reported interferometric observations in polarized light carried out with a polarimeter designed to be placed at the combined focus of an optical interferometer. By lab validation and observations of stellar calibrators, we show that instrumental polarization effects of the polarimeter itself and of the whole instrument are very small and do not damage the interferometric performance by a strong contrast decrease at wide hour angles. Even if refining the study and investigating the visibility difference more deeply between two orthogonal polarizations would require a better signal-to-noise ratio, these observations clearly validate our previous modelling of the instrumental polarization (Rousselet-Perraut et al. 1996), as well as our design of the field-rotator compensator (Rousselet-Perraut et al. 1998).

For next generation instrumentation, we emphasize that adding a polarimetric mode to an interferometric array enhances its ability to probe and study circumstellar environments. This requires paying attention to instrumental polarization during the concept study of the interferometric instrument, which is mandatory anyway for classical interferometry to avoid a visibility decrease due to instrumental polarization cross-talk. Circular and linear polarization analyses are very useful, and *simultaneous* recording of the two orthogonal polarizations is required to cross-correlate them (Chesneau et al. 2001). Such polarimetric equipment is also a powerful means for accurately calibrating any visibility measurement by allowing the various sources of instrumental bias to be disentangled and, as such, it is very attractive within the context of very high accuracy measurements.

Acknowledgements. The authors want to warmly thank C. Cazalé for the polarimeter manufacturing, as well as O. Absil and J.C. Augereau for fruitful discussions about the debris disk of α Lyr. The authors would like to thank the referee whose suggestions and comments greatly improved the paper's clarity. They are also grateful to the French Programs PNPS, PNST, and CNRS/ATI for funding the project.

References

Absil, O., et al. 2006, A&A, submitted
Berio, P., Mourard, D., Bonneau, D., et al. 1999, J. Opt. Soc. Amer. A, 16, 872
Chesneau, O., Rousselet-Perraut, K., Vakili, F., et al. 2000, in Interferometry in Optical Astronomy, SPIE Conf., ed. A. Quirrenbach, & P. Léna, Proc. SPIE, 4006, 531
Chesneau, O., Vakili, F., Rousselet-Perraut, K., & Stehlé, C. 2001, in Magnetic fields across the Hertzsprung-Russell diagram, ed. G. Mathys, S. K. Solanki, & D. T. Wickramasinghe, ASP Conf., 248, 633
Chesneau, O., Wolf, S., & Domiciano de Souza, A. 2003, A&A, 410, 375
Collett, E. 1992, Polarized light, Fundamentals and applications (New York: Marcel Dekker)
Elias, N. 2004, ApJ, 611, 1175
Hanbury Brown, R., Davis, J., & Allen, L. R. 1974, MNRAS, 168, 93
Ireland, M., Tuthill, P., Davis, J., & Tango, W. 2005, MNRAS, 361, 337
Mourard, D., Tallon-Bosc, I., Rigal, F., et al. 1994, A&A, 288, 675
Mourard, D., Bonneau, D., Stee, P., et al. 2003, in Interferometry for Optical Astronomy II, ed. W. Traub, SPIE Conf., August 2002, Hawaii, 4838, 9
Rousselet-Perraut, K., Vakili, F., & Mourard, D. 1996, Optical Engineering, 35, 2943
Rousselet-Perraut, K., Vakili, F., Mourard, D., et al. 1997, A&AS, 123, 173
Rousselet-Perraut, K., Hill, L., Lasselin-Waultier, G., et al. 1998, Opt. Eng., 37, 610
Rousselet-Perraut, K., Stehlé, C., Lanz, T., et al. 2004, A&A, 422, 193
Tinbergen, J. 2003, in Polarimetry in Astronomy, ed. S. Fineschi, SPIE Conf., August 2002, Hawaii, 4843, 122
Vakili, F. 1981, A&A, 101, 352
Vakili, F., Mourard, D., Bonneau, D., et al. 1997, A&A, 323, 183
van Belle, G., Ciardi, D., ten Brummelaar, T., et al. 2005, AJ, in press

Online Material

Appendix A: Laboratory qualification

The main characteristics of the polarimetric mode were checked and/or studied during July 2002 with the fringe simulator:

1. When the quarter waveplate was introduced, the interferogram positions on the detector remained the same within ±1 pixel, i.e. within a fraction 1/14 of the Airy disk.
2. When the Wollaston prism rotated from 0° to 180°, the interferogram spacing on the detector remained constant but their absolute positions vary by 22–25 pixels, which corresponds to a 1.6–1.8 Airy disk. A light eccentricity occured during the Wollaston rotation. Given this shift in the interferogram position, we only used the 0°-position of the Wollaston prism.
3. No spectral shift was detected whatever the configuration (with or without the polarimeter, when the Wollaston rotates, with or without the quarter waveplate). Note that accurate spectral calibration is also possible with both the polarimetric mode and a spectral lamp, as for classical observations.
4. When the linear sheet-film polarizer was inserted, one of the two interferograms observed after the Wollaston prism vanished. The 90°-rotation of the linear sheet-film polarizer leaded the other interferogram to vanish. This cancelling was measured at the accuracy of the detector dynamic, i.e. 4×10^{-3}. No cross-talk effects between the two orthogonal polarization directions larger than 4×10^{-3} were detected.
5. The flux of the *High* interferogram was always larger than that of the *Low* interferogram. A flux ratio *High*/*Low* between 1.78 and 1.15 was recorded around $\lambda = 0.65\ \mu$m with and without the quarter waveplate. This shows that a vignetting effect occured for the *Low* beam.
6. The *High* and *Low* visibilities were well-balanced and the difference smaller than our 5% rms fluctuations, whatever the polarization of the incident light and the analysis mode (Table A.1).
7. Two orthogonal polarization directions were generally transmitted differently and phase-shifted by an interferometer. Moreover, inside an asymmetric Coudé train, these instrumental effects differed from one interferometric arm to another. As a consequence, a polarization direction leaded to fringe patterns that could be shifted by instrumental effects with respect to those coming from the other polarization direction. In a classical mode of observations, the fringes resulting from the sum of all these patterns are recorded and the contrast is damaged by the superposition of the phase-shifted patterns. In such a case, selecting only one polarization direction generally allows significant improvement in the measured contrast. In our case, we tested instrumental polarization by inserting a linear sheet-film polarizer at the spectrograph entrance. No significant improvement of the visibility was detected, proving that no drastic effect of the instrumental polarization was observed.

Table A.1. *High* and *Low* polarized visibilities measured with the lab workbench and the polarimetric mode of the GI2T/REGAIN. The instrumental configuration is given by the presence of the quarter waveplate (Col. 2), and by the presence and the orientation (H = horizontal, V = vertical) of the linear sheet-film polarizer (Col. 3). We distinguish two modes (Col. 1): one for analyzing the linear polarizations and one for analyzing the circular ones. The central wavelength is 660 nm, the grating is 300 gr/mm, and the Wollaston prism position is the 0° one. Our statistical study leads to an rms fluctuations of our measurements of 5%.

Mode	Quarter Waveplate	Sheet-film Polarizer	$V_{\rm High}$	$V_{\rm Low}$
Linear analysis	0	–	0.23	0.21
"	0	V	0.28	NA
"	0	H	NA	0.26
Circular analysis	1	–	0.25	0.23
"	1	V	0.26	0.26
"	1	H	0.21	0.22

Appendix B: Data processing

This section outlines the main steps of the data-processing method of Mourard et al. (1994).

B.1. Individual energies

– We first correct the (x, λ) image for geometrical distorsions. This image is composed of either a naturally dispersed fringe pattern centered on the detector or of two polarized dispersed fringe patterns placed at the top and the bottom of the detector (Fig. B.1a).
– We compute the average autocorrelation of the spectral and spatial windows of the image. We define three identical geometrical windows for the *Nat*, *High*, and *Low* measurements, respectively (Fig. B.1a). The choice of identical sizes for the three windows leads to relatively small windows with respect to the whole detector size and to different flux levels for the three kinds of measurements.
– We compute the spectral density by a 2D Fourier Transform of the autocorrelation (Fig. B.1b) and correct for the centroiding hole, as well as for the photon bias as explained in Bério et al. (1999). At this step, an incorrect centroiding hole correction leads to features in the background of the spectral density and thus to a strong bias in the visibility estimation. Due to a recent change of the REGAIN detectors, this interpolation must be optimized for the new camera configuration and validated on various sets of data and various shapes of spectral and spatial windows. In our case, we fixed the correction parameters by minimizing the residual features in the spectral density background in the two sets of data. An optimization of these parameters is difficult because of using reduced windows for data processing. This obliges us to define a visibility estimator that is less sensitive to this correction and to define quality criteria to check this estimation (see subsections below).
– We estimate the energy of the high-frequency peak (or fringe peak) $E_{\rm HF}$, the energy of the low-frequency peak $E_{\rm LF}$, the energy of the speckle peak $E_{\rm SP}$. For each estimation we check that the background is properly subtracted and that the energies are unbiased. For the $E_{\rm HF}$ estimation, we use the following procedure (Fig. B.1c):
  1. we search the fringe peak across the spectral density by a maximum detection;
  2. we determine the peak width that can be larger than 1 pixel due to peak distortion. Typically we obtain a peak width of 3 pixels;
  3. we fit the spectral density background with a third-order polynomial over a wide range around the fringe peak but excluding the latter;
  4. we integrate the energy below the fringe peak $E_{\rm HF}$ after the background correction.

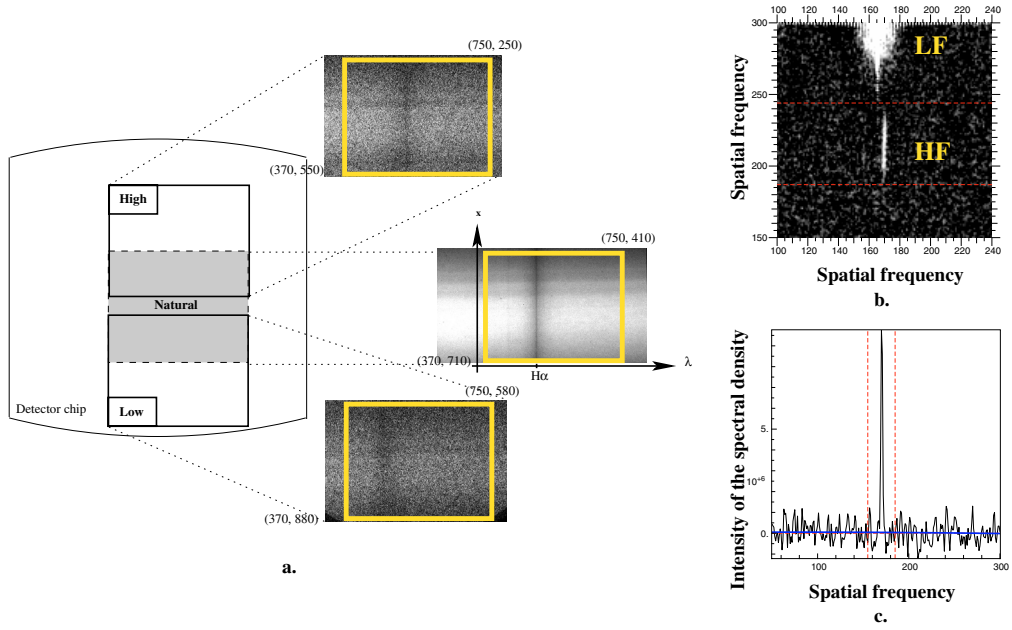

Fig. B.1. a) Long-exposure images of α Lyr. Spectral and spatial windows used for computation of the average autocorrelation are displayed by large rectangles in thick lines. **b)** Spectral density with the low-frequency LF and high-frequency HF contributions. **c)** Estimation of the energy of the high frequency peak $E_{\rm HF}$ (see text for details).

B.2. Statistical analysis

To check the consistency of a set of estimated energies, we plot $E_{\rm HF}$ and $E_{\rm SP}$ versus $N_{\rm ph}^2$ where $N_{\rm ph}$ stands for the photon number in the image. A bad fit of the speckle peak (the case for file #1 of α Lyr) or of the fringe peak (cases for files #5 and #7 of α Cep and for file #1 of α Lyr) can thus be detected and flagged. A normalization factor *Cor* can also be defined for the visibility computation by a polynomial fit of $E_{\rm SP}$ versus $N_{\rm ph}^2$.

B.3. Visibility estimator

When the energies are correctly computed and checked, we define the squared visibility as:

$$\mu^2 = \frac{2E_{\rm HF}}{N_{\rm ph}^2 \times {\rm Cor}} \qquad \text{(B.1)}$$

where Cor is the normalization factor.

No correction for differential photometry in the two arms of the interferometer is applied. If anything, we finally correct the visibility for the lateral displacement of the pupils. In fact, during the observations of α Cep, the pupil stabilization fails, thereby inducing a tilt of the fringes on the spectrograph slit and thus a visibility decrease.

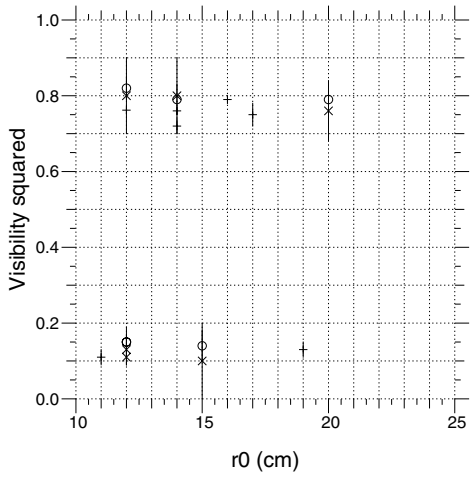

Fig. B.2. Squared visibility versus Fried parameter r_0 measured on α Cep (*top*) and on α Lyr (*bottom*) observations: *Natural* (+), *High* (∘), and *Low* (×) visibilities derived with the spectral and spatial windows defined in Fig. B.1a. For clarity, the visibilities squared of α Cep are shifted by 0.5.

B.3.1. Estimator bias

- Our visibility estimator depends upon the shape of the spectral and spatial window defined in the image for the autocorrelation computation. Since we pay attention to use windows of identical sizes for the three kinds of observations (*Nat*, *High* and *Low* polarizations) for each target, visibilities of a given target can be compared between them. But since we use windows for α Lyr that are larger than for α Cep, we cannot compare the results of both targets.
- To tackle the problem of centroiding hole correction, we define an estimator that is not based on the energy of the low frequency peak, $E_{\rm LF}$. This estimator is turbulent, which prevents us from comparing α Cep ($\delta = 62°35'$) with α Lyr ($\delta = 38°47'$) data and from discussing the absolute values of visibility. Nevertheless the plot of the visibility squared versus the Fried parameter r_0 measured during the observations shows no clear correlation (Fig. B.2).
- We check the set of α Cep data, including 11 visibility points, to make certain that our visibility estimator is not biased by the photon number (Fig. B.3). Nevertheless, the centroiding hole correction varies with the photon number, so the background correction is different for both targets.

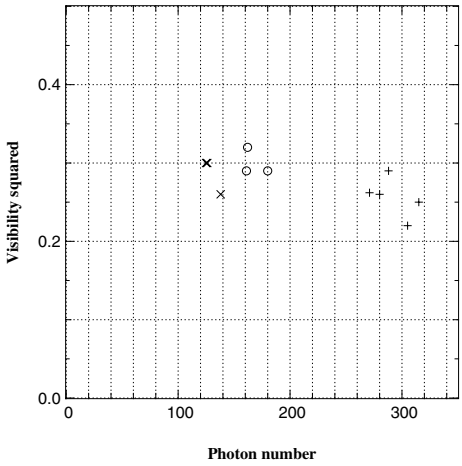

Fig. B.3. Squared visibility versus photon number per image computed on α Cep observations: *Natural* (+), *High* (∘), and *Low* (×) visibilities derived with the spectral and spatial windows defined in Fig. B.1a.

B.3.2. Error bars

Our estimator is affected by the accuracy of the high-frequency energy estimation and by the fluctuations of the photon number. We compute those rms fluctuations in the spectral-density background near the fringe peak (Fig. B.1c) that dominate the visibility error bar.